Arch. Mech., **68**, 6, pp. 487–513, Warszawa 2016

A minimal gradient-enhancement of the classical continuum theory of crystal plasticity. Part II: Size effects

S. STUPKIEWICZ, H. PETRYK

Institute of Fundamental Technological Research
Polish Academy of Sciences
Pawińskiego 5B
02-106 Warsaw, Poland
e-mails: sstupkie@ippt.pan.pl, hpetryk@ippt.pan.pl

In our previous paper, a simple gradient-enhancement of the classical continuum theory of plasticity of single crystals deformed by multislip has been proposed for incorporating size effects. A single internal length scale has been derived as an explicit function of the flow stress defined as the isotropic part of critical resolved shear stresses. The present work is focused on verification whether the simplifications involved are not too severe and allow satisfactory predictions of size effects. The model has been implemented in a finite element code and applied to three-dimensional simulations of fcc single crystals. We have found that the experimentally observed indentation size effect in a Cu single crystal is captured correctly in spite of the absence of any adjustable length-scale parameter. The finite element treatment relies on introducing non-local slip rates that average and smoothen on an element scale the corresponding local quantities. Convergence of the finite element solution to the analytical one is also verified for the one-dimensional problem of a boundary layer formed at a constrained interface.

Key words: gradient plasticity, geometrically necessary dislocations, boundary layer, size effects, indentation, finite element method.

1. Introduction

In Part I [1] of this paper, a novel 'minimal' framework of gradient-enhanced plasticity of metal single crystals at arbitrary deformation has been developed. The aim was to capture the effect of slip-rate gradients in a possibly simple manner consistent with phenomenological laws established in materials science. This has been done in the framework of classical continua, using balance equations in the most standard form only, avoiding thus a dilemma concerning the choice between alternative higher-order theories. The essence of the proposed modification of the classical theory of crystal plasticity is in extending only the evolution equations for critical resolved shear stresses, by a single non-conventional term

T. A. Kowalewski acted as Editor for this manuscript.

involving slip-rate gradients. That gradient-enhancement of the conventional theory is called 'minimal' as it can hardly be simplified further. Selected references to the vast literature on other gradient theories of crystal plasticity and on the related background from materials science can be found in Part I. The reader is also referred to Part I for the details of the derivation of the model used here.

As one of the major results of Part I, the derived internal length scale ℓ has been expressed through standard quantities that appear in a non-gradient hardening law. Hence, for a given conventional model of crystal plasticity without size effects, its gradient-enhancement is obtained automatically, as no further assumption is needed to define the characteristic length. Moreover, in the circumstances specified in Part I, the derived internal length scale possesses a direct physical interpretation that is frequently missing in other gradient-plasticity models.

The present paper is focused on verification whether the simplifications involved are not too restrictive, in particular, whether size effects are captured correctly. The primary challenge here is to verify soundness of the predicted indentation size effect by comparison with experimental observations. Satisfactory prediction of size effects is crucial for validation of the model in which the internal length scale is varying with the flow stress in a definite manner and thus cannot be used for fitting purposes. The indentation size effect has been selected for such validation since indentation is one of best-known size-dependent tests, cf. NIX and GAO [2]. In Section 4.4, the results of 3D finite element (FE) simulations of spherical indentation in a single crystal of high-purity copper are compared with experimental data taken from the literature. This is preceded, in Sections 4.1–4.3, by the analytical and numerical study of boundary layers at constrained interfaces and of convergence of the FE solution to the analytical one.

It is pointed out that FE implementation of the model is not a routine one because the model involves slip-rate gradients that are not available in a typical implementation of crystal plasticity. In particular, it is not immediate how to impose appropriate boundary constraints on slip-rates. Moreover, spatial jumps in slip-rate gradients are not excluded in general, so that irregular solutions can be expected in addition to smooth ones. Therefore, a kind of regularization is required to perform computations effectively. In the proposed FE treatment, non-local slip-rates are introduced as additional global unknowns that average and smoothen on an element scale the local slip-rates evaluated at element Gauss points. The plastically convected derivative of the dislocation density tensor is then computed in terms of those non-local slip-rates. Feasibility of this formulation is verified against an analytic solution of a boundary layer problem formulated for a constrained half-space.

2. Summary of the gradient-enhanced crystal plasticity model

The 'minimal' gradient-enhancement of the classical incremental hardening law of crystal plasticity has been summarized in Box I of Part I [1]. When incorporated in the standard set of equations governing the rate-boundary value problem of crystal plasticity, it generates the model used here. For convenience of the reader, the set of basic equations of the model is repeated below. The reader is referred to Part I for a more detailed description and for references to the literature.

2.1. Classical continuum deformed plastically by multislip

The standard multiplicative decomposition is adopted

$$\mathbf{F} = \mathbf{F}^*\mathbf{F}^{\mathrm{p}}, \qquad \mathbf{F}^* = \mathbf{R}^*\mathbf{U}^{\mathrm{e}}, \qquad (\mathbf{U}^{\mathrm{e}})^2 = \mathbf{C}^{\mathrm{e}} = \overset{\mathrm{T}}{\mathbf{F}}{}^*\mathbf{F}^*, \tag{2.1}$$

where $\mathbf{F}$ is the deformation gradient, $\mathbf{F}^{\mathrm{p}}$ is its plastic part and $\mathbf{F}^*$ is decomposed into elastic stretch $\mathbf{U}^{\mathrm{e}}$ and rotation $\mathbf{R}^*$ (see footnote 1 in Part I for the notation convention). Plastic deformation results from the collective effect of plastic slip on individual slip systems,

$$\dot{\mathbf{F}}^{\mathrm{p}} = \mathbf{L}^{\mathrm{p}}\mathbf{F}^{\mathrm{p}}, \qquad \mathbf{L}^{\mathrm{p}} = \sum_{\alpha} \dot{\gamma}_\alpha \, \mathbf{s}_\alpha \otimes \mathbf{m}_\alpha, \qquad \dot{\gamma}_\alpha \geq 0, \tag{2.2}$$

where $\mathbf{s}_\alpha$ and $\mathbf{m}_\alpha$ are fixed orthogonal unit vectors that specify the slip direction and slip-plane normal, respectively, and $\dot{\gamma}_\alpha$ is the corresponding plastic slip-rate, non-negative by convention (note, however, that the convention will be changed in the numerical treatment in Section 3). Normality flow rule can be expressed in the following subgradient form,

$$\mathbf{L}^{\mathrm{p}} \in \partial\{\mathbf{M} \mid \tau_\alpha \leq \tau_\alpha^{\mathrm{c}} \ \forall\alpha\}, \tag{2.3}$$

where the Mandel stress $\mathbf{M}$,

$$\mathbf{M} = \overset{\mathrm{T}}{\mathbf{F}}{}^*\mathbf{S}^*, \tag{2.4}$$

is defined in terms of the Piola stress tensor $\mathbf{S}^*$ taken relative to the intermediate local configuration as a function of $\mathbf{F}^*$. The (generalized) resolved shear stress τ_α on slip system α is most simply defined in terms of $\mathbf{M}$,

$$\tau_\alpha = \mathbf{M} \cdot (\mathbf{s}_\alpha \otimes \mathbf{m}_\alpha). \tag{2.5}$$

The evolution equations for the corresponding critical resolved shear stresses τ_α^{c}, that constitute the essence of the proposed gradient-enhancement, are recalled below.

2.2. The gradient-enhanced incremental hardening law

To account for the effect of slip-rate gradients, the standard slip-system incremental hardening rule $\dot{\tau}^{\rm c}_\alpha = \theta \sum_\beta q_{\alpha\beta}\dot{\gamma}_\beta$ is extended to

$$\dot{\tau}^{\rm c}_\alpha = \theta\Big(\sum_\beta q_{\alpha\beta}\dot{\gamma}_\beta + \ell\dot{\chi}\Big), \tag{2.6}$$

in which the slip-rate gradient effect is introduced through the effective slip-rate gradient $\dot{\chi}$ and characteristic length ℓ (to be specified below), while θ, the instantaneous isotropic hardening modulus, and $q_{\alpha\beta}$, the dimensionless parameters describing unequal hardening of distinct slip systems, are the parameters of a typical non-gradient hardening law that is recovered in the special case when $\ell\dot{\chi} = 0$.

In the specific form (2.6) of an anisotropic hardening law, the slip-rate gradients affect only the rate of flow stress τ defined as the isotropic part of critical resolved shear stresses,

$$\dot{\tau} = \theta\,(\dot{\gamma} + \ell\dot{\chi}) \tag{2.7}$$

where, as in the classical case, the effective slip rate $\dot{\gamma}$ is defined through

$$\dot{\gamma} = \sum_\alpha \dot{\gamma}_\alpha. \tag{2.8}$$

Consistently with phenomenological laws established in materials science, the flow stress τ is assumed to be a function of the total dislocation density ρ through the (generalized) Taylor formula

$$\tau = \tau_\rho(\rho) = a\mu b\sqrt{\rho}, \tag{2.9}$$

where, for a given material, the strengthening coefficient a, the elastic shear modulus μ and the Burgers vector modulus b are known parameters. As discussed in detail in Part I, the characteristic length ℓ is then found in the following explicit form,

$$\ell = \frac{{\rm d}\tau_\rho/{\rm d}\rho}{b\theta} = \frac{a^2\mu^2 b}{2\tau\theta}. \tag{2.10}$$

Note that ℓ has been defined through standard quantities that appear in a non-gradient hardening law. Furthermore, the internal length-scale ℓ has been shown in Part I to possess a physical interpretation.

The formula $(2.10)_2$ for the characteristic length ℓ involves the flow stress τ and the isothermal hardening modulus θ, the later representing classically the

derivative of τ with respect to the accumulated slip γ. It is convenient to specify θ by a constitutive function of τ,

$$\theta = \theta_\tau(\tau) = \theta_0 \left(1 - \frac{\tau}{\tau_{\max}}\right), \tag{2.11}$$

where the latter formula, adopted in the calculations, defines the Voce-type strain-hardening law in a non-gradient case, cf. equation (2.48) in Part I. On combining Eqs. $(2.10)_2$ and $(2.11)_2$, the internal length scale ℓ is finally found as an explicit function of τ only, with all constant parameters having a fully standard meaning.

To complete the model, the effective plastic slip-rate gradient $\dot{\chi}$ must be defined. In general, this scalar quantity can be assumed as a suitable function of slip-rate gradients $\nabla\dot{\gamma}_\alpha$, i.e. $\dot{\chi} = \varphi(\nabla\dot{\gamma}_\alpha)$. By referring to the dislocation density tensor $\mathbf{G}$ defined by CERMELLI and GURTIN [3] as a finite-strain counterpart of the classical NYE's [4] tensor in the small-strain framework, the effective slip-rate gradient $\dot{\chi}$ has been postulated in Part I in the following form,

$$\dot{\chi} = \|\overset{\diamond}{\mathbf{G}}\|\,, \qquad \overset{\diamond}{\mathbf{G}} = \sum_\alpha \mathbf{s}_\alpha \otimes (\nabla^{\#}\dot{\gamma}_\alpha \times \mathbf{m}_\alpha), \qquad \nabla^{\#}\dot{\gamma}_\alpha = \overset{-\mathrm{T}}{\mathbf{F}^{\mathrm{p}}}\,\nabla\dot{\gamma}_\alpha. \tag{2.12}$$

Here, $\|\cdot\|$ denotes the Euclidean norm and $\overset{\diamond}{\mathbf{G}}$ the plastically convected (Oldroyd) derivative of the dislocation density tensor $\mathbf{G}$, cf. [3], so that

$$\overset{\diamond}{\mathbf{G}} = \dot{\mathbf{G}} - \mathbf{L}^{\mathrm{p}}\mathbf{G} - \mathbf{G}\overset{\mathrm{T}}{\mathbf{L}^{\mathrm{p}}} = \mathbf{F}^{\mathrm{p}}\,\frac{\partial}{\partial t}\Big(\overset{-1}{\mathbf{F}^{\mathrm{p}}}\mathbf{G}\overset{-\mathrm{T}}{\mathbf{F}^{\mathrm{p}}}\Big)\overset{\mathrm{T}}{\mathbf{F}^{\mathrm{p}}}. \tag{2.13}$$

In the small-strain framework, which will be employed to derive an analytical solution in Section 4.1, the effective slip-rate gradient $\dot{\chi}$ is defined as the norm of the rate of Nye's dislocation density tensor $\boldsymbol{\alpha}$, thus $\dot{\chi} = \|\dot{\boldsymbol{\alpha}}\|$, see equation (2.59) in Part I. In fact, formula (2.12) provides a consistent generalization of that definition to the finite-strain format.

The gradient-enhanced incremental hardening law (2.6) introduces, through definition (2.12), slip-rate gradients $\nabla\dot{\gamma}_\alpha$ into the standard set of equations governing the rate-boundary value problem of crystal plasticity.

3. Numerical implementation

Numerical implementation of the model developed in Part I and briefly described above has been carried out using the finite element (FE) method. The most important aspects of the FE implementation are briefly outlined in this section. For brevity, standard details are omitted.

3.1. Computation and regularization of slip-rate gradients

The present model is formulated in the framework of classical continua, and as such it does not involve additional balance equations, in spite of the slip-rate gradients involved in the constitutive equations. As shown later in Section 4.1, an analytical solution describing the boundary layer in a constrained half-space can be found directly with no additional treatment, just using Eqs. (2.6)–(2.12) in the isotropic-hardening small-strain version, and imposing the boundary constraint $\dot{\gamma}_\alpha = 0$. However, in a FE implementation of the model, computation of slip-rate gradients and imposing boundary constraints on slip-rates constitutes the main difference (and challenge) with respect to usual implementations of non-gradient crystal plasticity models.

A special treatment is also needed for another reason. As illustrated in Section 4.1, see Eq. (4.6) and the related discussion, the set of assumptions introduced does not ensure uniqueness of the incremental solution to a boundary-value problem. Spatial jumps in $\nabla\dot{\gamma}_\alpha$ are not excluded in general, so that irregular solutions can be expected in addition to smooth ones. A kind of regularization is thus required to avoid undesired oscillatory solutions.

In the standard FE setting of crystal plasticity, slip rates $\dot{\gamma}_\alpha$, or the corresponding increments $\Delta\gamma_\alpha$, are determined locally and independently at each integration (Gauss) point. This approach is also followed here so that the proposed gradient enhancement can be combined with an arbitrary implementation of multislip crystal plasticity (non-regularized or regularized, rate-dependent or rate-independent, etc.). The possibility of determining the necessary slip-rate gradients locally within individual elements using the Gauss-point values of slip rates, e.g. [5], has been rejected because this approach is not suitable for low-order (linear) elements nor for constraining the slip rates on the boundary. The popular mixed formulation, e.g. [6–8], in which slip gradients or related quantities are introduced as independent variables, has also been considered. However, initial trials have turned unsuccessful, possibly because the scheme itself does not introduce any regularization of slip-rate gradients. Similarly, the regularization effect is missing in the approach based on introducing a global continuous approximation of the Gauss-point slip rates using Lagrange multipliers or the penalty method, e.g. [9].

The proposed FE treatment, which meets the requirements mentioned in the first two paragraphs of this subsection, relies on introducing *non-local* slip rates $\bar{\dot{\gamma}}_\alpha$ that provide a global continuous approximation of the corresponding local slip rates $\dot{\gamma}_\alpha$. This is achieved by averaging the local slip rates $\dot{\gamma}_\alpha$ through the following partial differential equation (PDE) that is solved for each slip system α,

$$\bar{\dot{\gamma}}_\alpha - l_h^2 \nabla^2 \bar{\dot{\gamma}}_\alpha = \dot{\gamma}_\alpha, \tag{3.1}$$

where ∇^2 denotes the Laplace operator, and l_h is a numerical parameter of the dimension of length. The numerical length-scale l_h is assumed to be proportional to the size h of individual finite elements so that the above PDE provides *element-scale averaging and smoothing* of $\dot{\gamma}_\alpha$, independent of the physical length scale ℓ in the proposed gradient-enhancement of crystal plasticity.

The above equation (3.1) is inspired by the so-called *implicit-gradient model* frequently employed in damage mechanics and softening plasticity, e.g. [10, 11]. In the related models, the averaging delivered by introducing the non-local variable provides a regularization of the ill-posedness that results from strain softening, and the implicit-gradient formulation has been shown to be particularly convenient as compared to alternative approaches. In contrast to the present FE treatment, in those implicit-gradient models the characteristic (intrinsic) length is considered as a material parameter that specifies the size of the region over which the local variable is averaged.

Two kinds of typical boundary conditions can be prescribed for the non-local slip rates,

$$\dot{\bar{\gamma}}_\alpha = 0 \qquad \text{or} \qquad \nabla\dot{\bar{\gamma}}_\alpha \cdot \mathbf{n} = 0, \tag{3.2}$$

which correspond to 'micro-clamped' and 'micro-free' conditions, respectively, with $\mathbf{n}$ denoting the unit outer normal to the boundary. Accordingly, the boundary constraint $\dot{\gamma}_\alpha = 0$ is introduced numerically through the boundary condition $(3.2)_1$ enforced on the non-local counterpart $\dot{\bar{\gamma}}_\alpha$.

The above formulation admits a standard FE treatment with C^0-continuous interpolation of the non-local variables, the gradient of which can be naturally evaluated and used in the gradient-enhanced model. In the FE implementation of the model, the rates $\dot{\bar{\gamma}}_\alpha$ and $\dot{\gamma}_\alpha$ are replaced by the respective increments $\Delta\bar{\gamma}_\alpha$ and $\Delta\gamma_\alpha$, see Section 3.3. The non-local variables $\Delta\bar{\gamma}_\alpha$ constitute global unknowns, while the local increments $\Delta\gamma_\alpha$ are the Gauss-point variables governed by the constitutive equations of crystal plasticity.

3.2. Rate-independent regularization of multislip crystal plasticity

In order to avoid the well-known problems related to non-uniqueness of selection of active slip systems in multislip crystal plasticity, the kinetic equation governing the slip rates $\dot{\gamma}_\alpha$ is adopted in the form

$$\dot{\gamma}_\alpha = \frac{\dot{\zeta}}{\tau_\alpha^{\mathrm{c}}} \left(\frac{\tau_\alpha}{\tau_\alpha^{\mathrm{c}}} \right)^{2m-1}, \tag{3.3}$$

where $m \gg 1$ is an integer, and $\dot{\zeta}$ is a plastic multiplier to be discussed below. In order to decrease the number of unknowns, slip-systems of the same slip-plane normal $\mathbf{m}_\alpha$ and opposite slip directions $\mathbf{s}_\alpha$ are not longer treated as distinct, in

contrast to Section 2 where the slip rates were assumed to be non-negative. In the present numerical treatment, the resolved shear stress τ_α and corresponding slip rate $\dot{\gamma}_\alpha$ can be both of either sign.

The plastic multiplier $\dot{\zeta}$ in Eq. (3.3) is here eliminated using a single yield condition [12, 13],

$$F = \left(\sum_\alpha \left(\frac{\tau_\alpha}{\tau_\alpha^{\mathrm{c}}} \right)^{2m} \right)^{1/(2m)} - 1 \leq 0, \tag{3.4}$$

which provides an approximation of the collection of Schmid-type yield conditions $|\tau_\alpha| \leq \tau_\alpha^{\mathrm{c}}$ formulated for all individual slip systems. This leads to a *rate-independent* multislip crystal-plasticity model that is governed by the following associated flow rule of Mandel's type [14] accompanied by the usual complementarity conditions,

$$\mathbf{L}^{\mathrm{p}} = \dot{\zeta} \frac{\partial F}{\partial \mathbf{M}} = \sum_\alpha \dot{\gamma}_\alpha \, \mathbf{s}_\alpha \otimes \mathbf{m}_\alpha, \qquad \dot{\zeta} \geq 0, \qquad \dot{\zeta} F = 0, \tag{3.5}$$

with $\dot{\gamma}_\alpha$ given by Eq. (3.3). The plastic multiplier $\dot{\zeta}$ is determined from the consistency condition $\dot{F} = 0$.

In spite of the noticeable analogy to the viscoplastic models of crystal plasticity with the popular power-law, e.g. [15, 16], the factor $\dot{\zeta}/\tau_\alpha^{\mathrm{c}}$ in Eq. (3.3) does not represent a given reference slip rate, rather, it is here solution-dependent and different for each slip system. Evidently, the minimal gradient-enhanced framework summarized in Section 2 can be combined equally well with the viscoplastic flow rule.

3.3. Incremental finite-step formulation

Incremental constitutive equations are obtained by applying the implicit backward-Euler scheme to all evolution equations and by enforcing all the governing equations to hold at the end of each time increment.

The incremental form of the flow rule $(3.5)_1$, see also Eq. (2.2), is obtained by applying the exponential map integrator [17, 18],

$$\mathbf{F}^{\mathrm{p}}_{n+1} = \exp\Big(\sum_\alpha \Delta\gamma_\alpha \, \mathbf{s}_\alpha \otimes \mathbf{m}_\alpha \Big) \mathbf{F}^{\mathrm{p}}_n \tag{3.6}$$

so that incompressibility of plastic flow is automatically satisfied. Here, $\Delta\gamma_\alpha = \dot{\gamma}_\alpha \Delta t$ denotes the slip increment corresponding to the time step $t_n \to t_{n+1} = t_n + \Delta t$, and the subscript n or $n+1$ indicates the time instant at which the quantity of evaluated. The increment $\Delta\gamma$ of the total plastic slip, cf. Eq. (2.8),

and the effective slip-increment gradient $\Delta\chi$, cf. Eq. (2.12), are given by

$$\begin{aligned} \Delta\gamma &= \sum_\alpha |\Delta\gamma_\alpha|, \\ \Delta\chi &= \Big\| \sum_\alpha \mathbf{s}_\alpha \otimes (\nabla^\#(\Delta\bar\gamma_\alpha) \times \mathbf{m}_\alpha) \Big\|, \\ \nabla^\#(\Delta\bar\gamma_\alpha) &= \overset{-\mathrm{T}}{\mathbf{F}}{}^{\mathrm{p}}_{n+1}\, \nabla(\Delta\bar\gamma_\alpha). \end{aligned} \tag{3.7}$$

Note that $\Delta\chi$ is determined in terms of the gradients of non-local slip increments $\Delta\bar\gamma_\alpha$, as discussed in Section 3.1.

The hardening modulus θ_{n+1} is related to the isotropic part τ_{n+1} of the critical resolved shear stress and to the current internal length-scale ℓ_{n+1}, cf. Eqs. (2.7), (2.11) and (2.10), by

$$\begin{aligned} \tau_{n+1} &= \tau_n + \theta_{n+1}(\Delta\gamma + \ell_{n+1}\Delta\chi), \\ \theta_{n+1} &= \theta_\tau(\tau_{n+1}), \\ \ell_{n+1} &= \frac{a^2\mu^2 b}{2\tau_{n+1}\theta_{n+1}}, \end{aligned} \tag{3.8}$$

and the anisotropic hardening law (2.6) takes the form

$$\tau^{\mathrm{c}}_{\alpha,n+1} = \tau^{\mathrm{c}}_{\alpha,n} + \theta_{n+1}\Big(\sum_\beta q_{\alpha\beta}\Delta\gamma_\beta + \ell_{n+1}\Delta\chi \Big). \tag{3.9}$$

Note that the internal length-scale ℓ enters the model only through the product $\theta\ell$. Therefore, in the numerical calculations, only the product $\theta_{n+1}\ell_{n+1}$ is actually computed to avoid ill-posedness of ℓ_{n+1} when $\theta_{n+1} \to 0$.

Finally, in view of Eq. (3.3), slip increments $\Delta\gamma_\alpha$ are related to the respective current resolved shear stresses $\tau_{\alpha,n+1}$ by

$$\Delta\gamma_\alpha = \frac{\Delta\zeta}{\tau^{\mathrm{c}}_{\alpha,n+1}} \left(\frac{\tau_{\alpha,n+1}}{\tau^{\mathrm{c}}_{\alpha,n+1}} \right)^{2m-1}, \qquad \tau_{\alpha,n+1} = \mathbf{M}_{n+1} \cdot (\mathbf{s}_\alpha \otimes \mathbf{m}_\alpha), \tag{3.10}$$

where the Mandel stress $\mathbf{M}_{n+1}$ is derived from the elastic strain energy function $W(\mathbf{C}^{\mathrm{e}})$. Since elastic strains are small in ductile crystals, the elastic response is simply assumed to be governed by the anisotropic St. Venant–Kirchhoff model so that we have

$$W = \frac{1}{2}\,\mathbf{E}^{\mathrm{e}} \cdot \mathbb{L}\mathbf{E}^{\mathrm{e}}, \qquad \mathbf{E}^{\mathrm{e}} = \frac{1}{2}(\mathbf{C}^{\mathrm{e}} - \mathbf{1}), \qquad \mathbf{M} = 2\mathbf{C}^{\mathrm{e}}\frac{\partial W}{\partial \mathbf{C}^{\mathrm{e}}}, \tag{3.11}$$

where $\mathbb{L}$ is a given fourth-order elastic stiffness tensor.

For illustration purposes, the dislocation density tensor $\mathbf{G}$ will also be computed. Since $\overset{\diamond}{\mathbf{G}}$ defined by Eq. $(2.12)_2$ is the plastically convected (Oldroyd) derivative (2.13) of $\mathbf{G}$, the following update formula is obtained upon application of the backward-Euler scheme in the reference configuration followed by a push-forward to the local intermediate configuration,

$$\begin{aligned} \mathbf{G}_{n+1} &= \mathbf{f}^{\mathrm{p}}_{n+1}\mathbf{G}_n\overset{-\mathrm{T}}{\mathbf{f}^{\mathrm{p}}_{n+1}} + \sum_\alpha \mathbf{s}_\alpha \otimes (\nabla^{\#}(\Delta\bar{\gamma}_\alpha)\times\mathbf{m}_\alpha), \\ \mathbf{f}^{\mathrm{p}}_{n+1} &= \mathbf{F}^{\mathrm{p}}_{n+1}\overset{-1}{\mathbf{F}^{\mathrm{p}}_{n}}. \end{aligned} \tag{3.12}$$

The second term in the formula for $\mathbf{G}_{n+1}$ is recognized to appear also in Eq. (3.7) defining the effective slip-increment gradient $\Delta\chi$.

3.4. Finite element implementation

The implementation has been carried out using the *AceGen*/*AceFEM* system. *AceGen* is a code generation system that combines symbolic capabilities of *Mathematica* (www.wolfram.com) with an automatic differentiation (AD) technique and advanced expression optimization techniques [19]. Application of *AceGen* largely simplifies implementation of complex constitutive models thanks to the automation of otherwise tedious steps, like derivation and coding of the consistent tangent matrix. FE computations reported in Section 4 have been performed using *AceFEM*, a highly flexible FE code that is closely integrated with *AceGen*.

The formulation outlined in Sections 3.1–3.3 leads a computational scheme in which the global unknowns are the displacements and non-local slip increments. In three-dimensional problems, there are thus 15 degrees of freedom per node (3 displacements and 12 slip increments for fcc metals), and the nonlinear equations resulting from the FE discretization are solved simultaneously with respect to all unknowns using the Newton method. The tangent matrix required by the Newton method is obtained by exact linearization of the incremental constitutive equations including the coupling between the displacement-based formulation of crystal plasticity and the PDE governing the non-local slip increments.

Overall, the FE implementation has proven to be fairly robust so that 3D simulations of spherical indentation have been successfully carried out for a wide range of indenter radii, see Section 4.4. However, our experience shows that the convergence behaviour is sensitive to implementation details, such as regularization of the norm in the definition of $\Delta\chi$, see Eq. $(3.7)_2$. For instance, tuning of the algorithm was important for performing the convergence study reported in the next section.

4. Study of size effects

Three examples are analyzed below. The first and second examples are concerned with the problem of shearing of a constrained half-space and strip, respectively. These examples are intended to illustrate the proposed gradient-enhancement of crystal plasticity by the analysis of dimensional dependencies in boundary layers at constrained interfaces. Furthermore, the two examples are used for verification of the present FE formulation against an analytic solution. The third example is aimed to provide an answer to the major question whether the predicted size effect in indentation of a single crystal is captured correctly in comparison with experimental observations. That verification is essential for validation of predictive capabilities of the present approach since here no possibility is left for adjusting the internal length scale ℓ responsible for the size effect.

4.1. Boundary layer in a constrained half-space subjected to shear

In this section, shearing of a constrained half-space $y \geq 0$ is considered, see Fig. 1a. The half-space is subjected to a uniform shear stress $\sigma_{xy} \geq 0$, and plane-

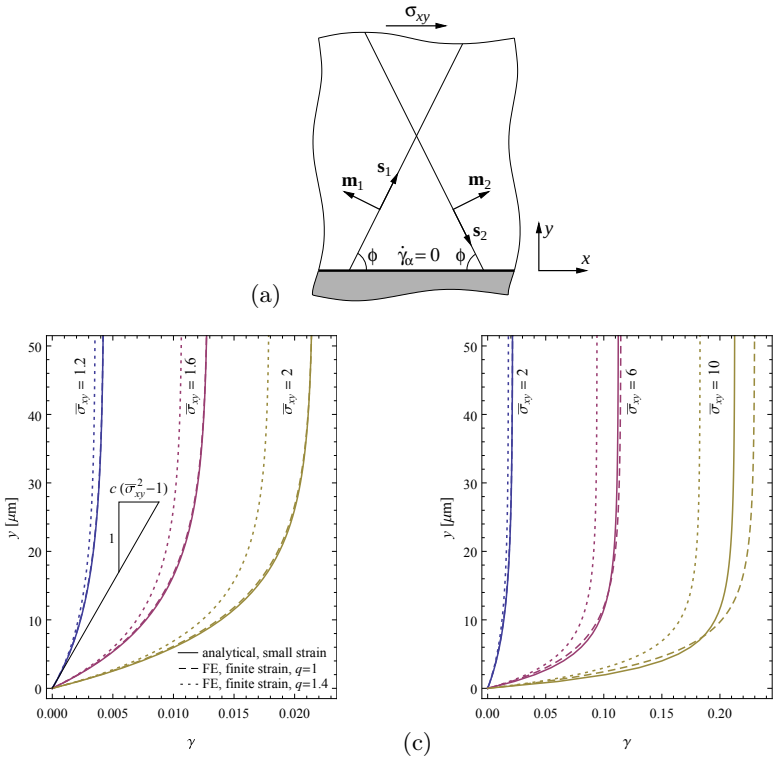

FIG. 1. Shearing of a constrained half-space: (a) schematic of the problem; (b,c) profiles of accumulated slip γ at relatively small (b) and moderate (c) strains.

strain conditions are assumed. For illustrative purposes, plastic deformation is assumed to result from activity of two slip systems, $\alpha = 1, 2$, oriented at an angle ϕ with respect to the interface, as shown in the figure. Plastic slip is constrained at the interface, thus $\dot\gamma_\alpha = 0$ at $y = 0$. A similar problem of a constrained half-space has been considered by HAN *et al.* [20], and a related problem of a constrained strip has been studied in numerous works, e.g., by SHU *et al.* [21], BITTENCOURT *et al.* [22], and others.

The Schmid-type rate-independent yield criterion $|\tau_\alpha| \le \tau_\alpha^{\rm c}$ is used directly since no constitutive regularization is needed in the present case of double-slip crystal plasticity. Material parameters are adopted as in the subsequent example of spherical indentation, see Table 1 in Section 4.4, except that, for simplicity, isotropic elasticity is here assumed with $\mu = 40.3$ GPa and $\nu = 0.34$. Orientation of slip planes is specified by $\phi = \pi/3$.

An analytical solution is derived below for the corresponding one-dimensional small-strain problem, which is also used to verify the convergence of the finite-strain FE results to the small-strain solution. The analytical solution requires that anisotropic hardening in the model defined in Section 2.2 is not included, thus $q = 1$ in the small-strain analysis, implying $q_{\alpha\beta} = 1$ in the hardening law (2.6).

The rotations are neglected in the small-strain framework so that symmetric orientation of the two slip systems is maintained throughout the deformation process. As a result, by symmetry, the resolved shear stresses and slip rates are identical on both slip systems, thus $\tau_1 = \tau_2 = \sigma_{xy}\cos 2\phi$, $\dot\gamma_1 = \dot\gamma_2$, and we have $\dot\gamma = 2|\dot\gamma_1|$.

The small-strain counterpart $\dot{\boldsymbol\alpha}$ of the incremental dislocation density tensor $\overset{\diamond}{\mathbf{G}}$ is given by Eq. $(2.12)_2$ on taking $\mathbf{F}^{\rm p}$ as the identity tensor. In the present case, the only non-zero component of $\dot{\boldsymbol\alpha}$ is $\dot\alpha_{yz} = 2\dot\gamma_1' \sin^2\phi$, and thus $\dot\chi = \|\dot{\boldsymbol\alpha}\| = 2|\dot\gamma_1'|\sin^2\phi$, where $\dot\gamma_1' = {\rm d}\dot\gamma_1(y)/{\rm d}y$.

The hardening law $\dot\tau_\alpha^{\rm c} = \dot\tau = \theta(\dot\gamma + \ell\dot\chi)$, cf. Eqs. (2.6) and (2.7), along with the yield condition $|\tau_\alpha| = \tau_\alpha^{\rm c}$ lead now to the following differential equation for the effective slip rate $\dot\gamma = \dot\gamma(y)$,

$$|\dot\gamma'| + \frac{1}{\ell_y}\,\dot\gamma = A\,\dot\sigma_{xy}, \qquad \ell_y = \ell\sin^2\phi, \qquad A = \frac{|\cos 2\phi|}{\theta\ell\sin^2\phi}, \tag{4.1}$$

for $\sigma_{xy} \ge \sigma_{xy,0}$ and $\dot\sigma_{xy} > 0$, where $\sigma_{xy,0} = |\cos 2\phi|\tau_0$ is the initial yield stress. Note that parameters ℓ and θ, and thus also ℓ_y and A, depend on the current critical resolved shear stress τ, but they do not depend on the position y. This is because the stress is constant within the half-space, thus $\tau_\alpha^{\rm c} = |\tau_\alpha| = \sigma_{xy}|\cos 2\phi|$ is also constant, and we have $\tau = \tau_\alpha^{\rm c}$ in the absence of anisotropic hardening ($q = 1$). This is actually the reason why anisotropic hardening has not been included in the small-strain model.

Assuming that the effective slip-rate $\dot\gamma$ increases monotonically from 0 at the interface as y increases, we have $\dot\gamma' > 0$, and thus $\dot\chi = \dot\gamma' \sin^2\phi$. The exact solution of the spatial differential equation (4.1) for $\dot\gamma' > 0$ with the boundary condition $\dot\gamma(0) = 0$ is immediate,

$$\dot\gamma = A\ell_y(1 - e^{-y/\ell_y})\dot\sigma_{xy}. \tag{4.2}$$

The effective slip rate $\dot\gamma$ is thus found as an exponential function of the distance from the interface with parameters ℓ_y and A specifying a conventional thickness of the (instantaneous) boundary layer and the asymptotic value far from the interface, respectively. It is worth emphasizing that it is the internal length-scale ℓ that plays (through ℓ_y) the crucial role in defining the slip-rate profile, as it specifies the boundary layer thickness. The accumulated slip γ is obtained by time integration of the rate $\dot\gamma$ given by Eq. (4.2) with time dependent parameters ℓ_y and A. The time integration is performed numerically.

The results are presented in Fig. 1b,c where they are compared with the FE results obtained for the finite-strain model without and with anisotropic hardening, for $q = 1$ and $q = 1.4$, respectively. As the model is rate-independent, the monotonically increasing stress σ_{xy} is adopted as a time-like parameter, and the solution is parameterized by the normalized stress $\overline\sigma_{xy} = \sigma_{xy}/\sigma_{xy,0}$.

The small-strain model (solid lines) and the geometrically-exact finite-strain model without anisotropic hardening (dashed lines) agree perfectly when the strains are relatively small, Fig. 1b. At larger strains, the corresponding results differ visibly, Fig. 1c, due to the finite-deformation effects, notably due to lattice rotation.

The effect of anisotropic hardening (dotted lines) is substantial regardless of the strain level. This is expected because, in the case of anisotropic hardening, the additional latent hardening increases the effective hardening modulus so that the accumulated slip γ at a fixed stress is reduced.

It is, however, interesting to note that the gradient of γ at $y = 0$ is identical in the three cases. This is because the plastic slip is constrained at $y = 0$ so that hardening is solely due to slip (rate) gradients, and additional latent hardening does not intervene. This also implies that there is no lattice rotation at $y = 0$, and thus finite deformations do not influence the solution at $y = 0$.

The derivative $\gamma' = \mathrm{d}\gamma/\mathrm{d}y$ at $y = 0$ can be determined analytically in closed form. From Eqs. (4.1) and (2.10) we have

$$\dot\gamma'(0) = A\dot\sigma_{xy} = \frac{2\cos^2 2\phi}{\sin^2\phi}\,\frac{1}{a^2\mu^2 b}\,\sigma_{xy}\dot\sigma_{xy}, \tag{4.3}$$

and time integration yields the following compact formula

$$\gamma'(0) = c\,(\overline\sigma_{xy}^2 - 1), \qquad c = \frac{\tau_0^2}{a^2\mu^2 b\sin^2\phi} = \frac{b\rho_0}{\sin^2\phi}, \tag{4.4}$$

where $\overline{\sigma}_{xy} = \sigma_{xy}/\sigma_{xy,0}$, $\sigma_{xy,0} = |\cos 2\phi|\tau_0$, and ρ_0 is the initial dislocation density corresponding to the initial value τ_0 of the flow stress. Note that the above formula (4.4) does not depend on the specific form of the hardening law $\theta = \theta_\tau(\tau)$.

A still more general formula for the slope $\gamma'(0)$ of the profiles of γ at the boundary is obtained by time integration of the equation $\dot{\tau}^{\rm c}_\alpha = \dot{\tau} \equiv (\mathrm{d}\tau_\rho/\mathrm{d}\rho)\dot{\rho} = (\mathrm{d}\tau_\rho/\mathrm{d}\rho)(\dot{\chi}/b)$ obtained from Eqs. (2.7) and $(2.10)_1$ in the special case when $\dot{\gamma}_\alpha \equiv 0$. In this way, at $y = 0$ we obtain the expression

$$\gamma'(0) = c\left(\frac{\rho(0)}{\rho_0} - 1\right) \tag{4.5}$$

which holds for arbitrary functions τ_ρ and θ_τ. If the Taylor formula $(2.9)_2$ is used for defining τ_ρ as in the preceding results then the fraction $\rho(0)/\rho_0$ can be replaced with $\overline{\sigma}^2_{xy}$, and formula (4.4) is recovered.

Finally, we point out that a general solution to Eq. (4.1) need not be smooth as above, but can also be composed of smooth segments that satisfy

$$\begin{aligned} \text{either} \quad & \dot{\gamma}' = c_1\, e^{-y/\ell_y} \quad && \text{for } \dot{\gamma}' > 0 \\ \text{or} \quad & \dot{\gamma}' = -c_2\, e^{y/\ell_y} \quad && \text{for } \dot{\gamma}' < 0, \end{aligned} \tag{4.6}$$

where $c_1 \geq 0$ and $c_2 \geq 0$ are integration constants. It can easily be checked that a solution to Eq. (4.1) can be constructed in that way such that $\dot{\gamma}(y)$ is a continuous function, implying continuity of $|\dot{\gamma}'|(y)$, but with abrupt changes of the sign of $\dot{\gamma}'(y)$ at the connection points. A particular case of such irregular solutions is considered in Subsection 4.3. The regularization method based on Eq. (3.1) helps in obtaining smooth solutions convergent to the analytical solution (4.2), see the discussion presented in the next subsection.

4.2. Boundary layer: convergence of the FE-based computational scheme

In this subsection, we illustrate the convergence of the proposed computational scheme based on the non-local slip rates, as introduced by Eq. (3.1). For that purpose, the smooth analytical solution derived in Section 4.1 for the boundary layer formed in a constrained half-space is used as a reference. Convergence is here studied in terms of the accumulated slip γ. In the FE model, γ is obtained by summing the non-local slip increments, $\Delta\gamma = \sum_\alpha |\Delta\bar{\gamma}_\alpha|$, and is linearly interpolated between the nodes. Recall that the analytical solution employs the small-strain model, while the FE solution is based on the finite-deformation model.

In order to reduce the effect of finite deformations, convergence has been studied for the shear strain γ_{xy} below 0.0025 and accumulated slip γ below

0.005, attained at the normalized shear stress $\overline{\sigma}_{xy} = 1.2$. In all cases, time integration has been performed with a shear stress increment of $\Delta\overline{\sigma}_{xy} = 0.1$ used in Section 4.1. The one-dimensional FE computations have been carried out in the domain of the height of $100\,\mu$m which is sufficient to accurately resolve the boundary layer of a smooth profile dependent on the current value of ℓ in the investigated range and formed in the vicinity of the constrained boundary at $y = 0$. As in the 3D model of spherical indentation, Section 4.4, piecewise-linear interpolation of the displacements and non-local slip increments has been used.

Figure 2a shows the profiles of the accumulated slip γ at $\overline{\sigma}_{xy} = 1.2$ obtained for the numerical parameter l_h equal to the element size h for varying h. It can be seen that the FE solution converges to the analytical one as the element size decreases. Actually, the analytical solution and the solutions corresponding to h equal to $2\,\mu$m and $1\,\mu$m can hardly be distinguished on the diagram.

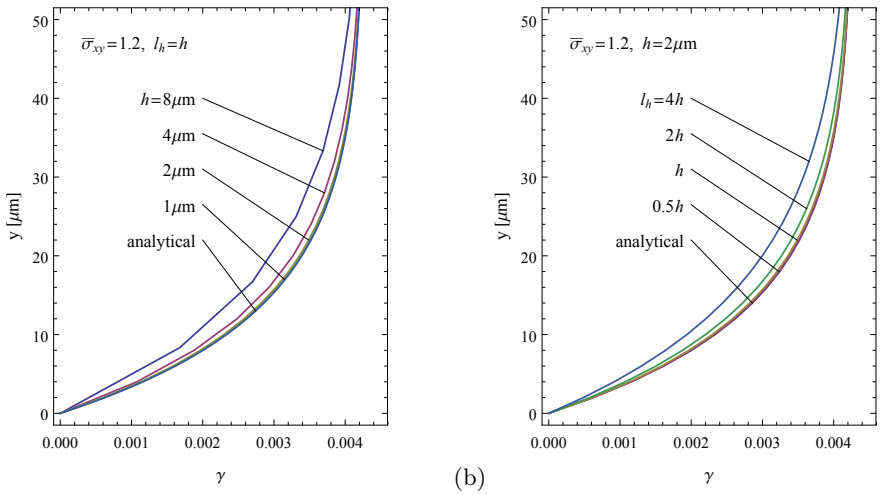

FIG. 2. Shearing of a constrained half-space: (a) profiles of accumulated slip γ for $l_h = h$ and for varying element size h; (b) profiles of accumulated slip γ for $h = 2\,\mu$m and for varying l_h.

Results corresponding to a fixed element size $h = 2\,\mu$m and l_h varying between $l_h = 4h$ and $0.5h$ are shown in Fig. 2b. It is apparent that with decreasing l_h the solution converges to the analytical one. A quantitative evaluation of the solution error is presented in Fig. 3 which shows the relative error in γ as a function of l_h in log-log scale. The relative error is defined here as the L_2 norm of the error in γ on the interval $0 \le y \le 100\,\mu$m normalized by the L_2 norm of γ. Four mesh densities are included in the figure, and l_h is in each case varied between $l_h = 0.5h$ and $l_h = 16\,\mu$m. The results indicate that the error is mainly governed by l_h, and the rate of convergence is close to 2. It has been checked that

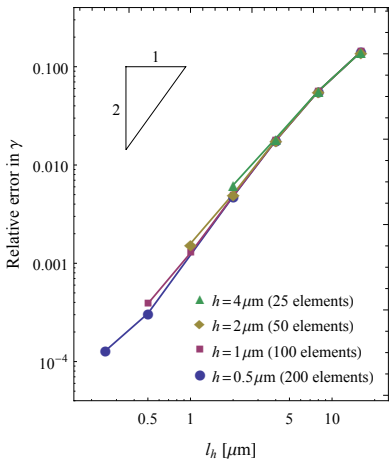

FIG. 3. Shearing of a constrained half-space: relative error in γ (L_2 norm) as a function of l_h and h.

the decrease in the convergence rate observed for $h = 0.5\,\mu$m and $l_h = 0.25\,\mu$m (the leftmost point in Fig. 3) results from the finite-deformation effects that are not included in the analytical solution.

4.3. Shearing of a constrained strip

In order to further illustrate the size effects predicted by the present model and the performance of the computational treatment based on Eq. (3.1), selected results are provided below for the problem of a constrained strip of thickness H, see Fig. 4a. As in the preceding subsections, the double-slip crystal-plasticity model is considered, but the constraint $\dot\gamma_\alpha = 0$ is now imposed on plastic slip both at $y = 0$ and at $y = H$. An analytical solution is constructed which is *assumed* to consist of *two* smooth segments corresponding to $\dot\gamma' > 0$ and $\dot\gamma' < 0$, see Eq. (4.6) and the related discussion in Section 4.1, with a jump in $\dot\gamma'$ at $y = H/2$.

The analytical solution is illustrated in Fig. 4b,c. Figure 4b shows the profiles of shear strain γ_{xy} corresponding to a fixed overall shear strain $\langle\gamma_{xy}\rangle = 0.05$ and for strip thickness H varying between 20 and 320 μm. The kink in the profile of γ_{xy}, which results from the jump in $\dot\gamma'$ at $y = H/2$, is clearly visible for small strip thickness H. As illustrated in Fig. 4c, the overall stress–strain response is size dependent due to the GND hardening effect that is more pronounced for small strip thickness H.

Convergence of the FE solution with decreasing characteristic length l_h is illustrated in Fig. 5a. The dashed line indicates the previous analytical solution in the constrained half-space. It is actually identical to a *smooth* solution for

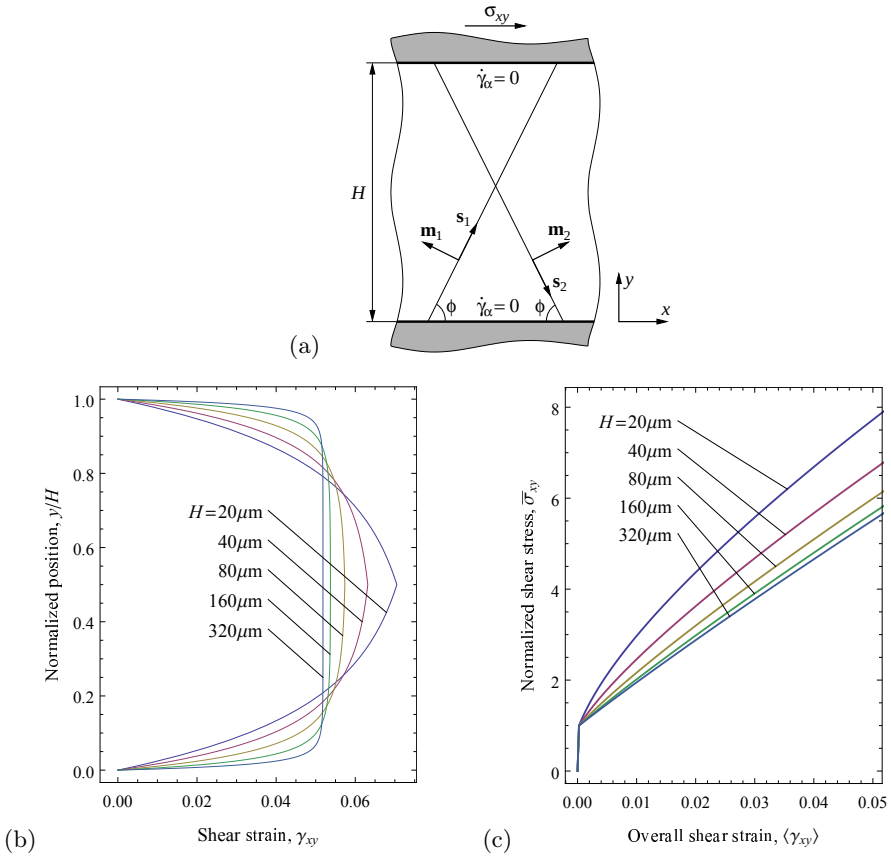

FIG. 4. Shearing of a constrained strip of thickness H: (a) schematic of the problem; (b) size-dependent profiles of shear strain γ_{xy} at fixed overall shear strain $\langle\gamma_{xy}\rangle = 0.05$; (c) normalized shear stress $\overline{\sigma}^2_{xy}$ as a function of overall shear strain $\langle\gamma_{xy}\rangle$ for varying H.

the strip with a constrained interface at $y = 0$ only and a fully unconstrained interface at $y = H$; alternative non-smooth solutions are not discussed here. In the FE solution, the kink in the profile of γ at $y = H/2$ is smoothed, however, with decreasing l_h the solution converges to the analytical one.

As both the analytical solution and the numerical one exhibit a kink in the profile of γ, the latter being smoothed at the element scale by Eq. (3.1), it is interesting to examine how the kink evolves with increasing shear stress and strain, and how the evolving kink is represented in the FE solution. This is illustrated in Fig. 5b which shows the profiles of the accumulated slip γ normalized by $\langle\gamma\rangle$, the average accumulated slip in the layer. It is apparent that the kink becomes *less* pronounced for increasing stress $\overline{\sigma}_{xy}$. This is because the internal length scale ℓ decreases with increasing stress within the examined range, and so does the apparent thickness of the instantaneous boundary layer, cf. Eqs. (4.2) and $(4.1)_2$.

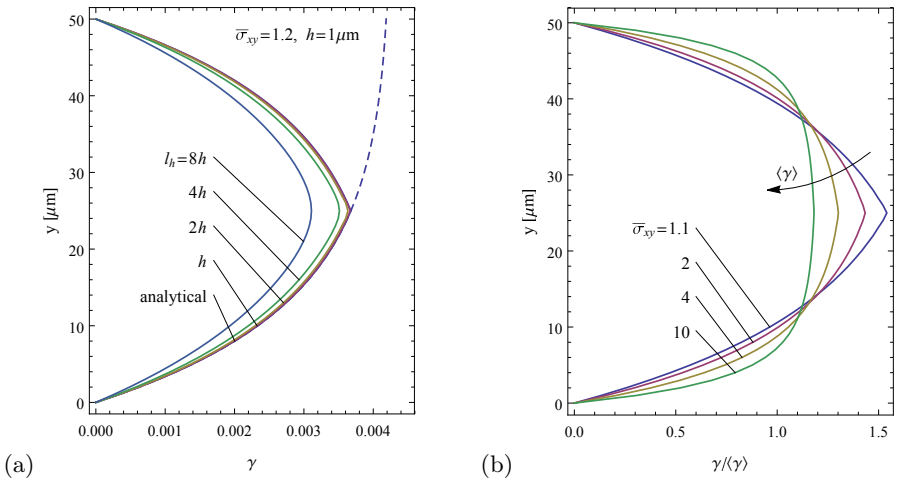

FIG. 5. Finite-element simulations of shearing of a constrained strip of thickness $H = 50\,\mu$m: (a) profiles of accumulated slip γ for $\overline{\sigma}_{xy} = 1.2$ and for varying l_h at fixed $h = 1\,\mu$m; (b) evolution of normalized accumulated slip $\gamma/\langle\gamma\rangle$ with increasing stress $\overline{\sigma}_{xy}$ and average accumulated slip $\langle\gamma\rangle$ (here $h = l_h = 1\,\mu$m).

4.4. Finite element simulation of spherical indentation

As the major example, FE simulations of spherical indentation in a (001)-oriented single crystal of copper have been carried out, and the results are reported in this section. The indenter radius R has been varied between $2\,\mu$m and $500\,\mu$m. The ratio of the maximum penetration depth $h_{\max}$ to the indenter radius has been kept constant, $h_{\max}/R = 0.11$, hence the deviations of the solutions from self-similarity are solely due to size effects introduced by the gradient-enhanced model proposed in this work. The adopted ratio of $h_{\max}/R = 0.11$ allows comparison to experimental results reported by KUCHARSKI *et al.* [23] for two indenter radii of $5\,\mu$m (maximum load of 10 mN) and $190\,\mu$m (nominal radius $200\,\mu$m, maximum load of 8 N), as presented below.

Material parameters used in the simulations are provided in Table 1. The parameters can be divided into three groups. Standard elastic constants (c_{11}, c_{12}, c_{44}) of a copper single crystal of cubic symmetry have been adopted from the literature.

Table 1. Material parameters used for high-purity copper single crystal.

c_{11}	c_{12}	c_{44}	τ_0	$\tau_{\max}$	θ_0	q	m	a	μ	b
170 GPa	124 GPa	75 GPa	5 MPa	240 MPa	240 MPa	1.4	20	0.33	40.3 GPa	0.256 nm

Hardening parameters (τ_0, $\tau_{\max}$, θ_0) have been calibrated using the results of spherical indentation reported in [23]. Specifically, the load–penetration P–h

curve corresponding to $R = 190\,\mu$m and to crystal orientation C1, which is close to (001), see [23], has been used for that purpose. The crystal plasticity model with the gradient effect *neglected* has been used in the simple calibration procedure of the model for $R = 190\,\mu$m as outlined below. First, considering that the copper single crystal is of high purity, a low value of the initial critical resolved shear stress, $\tau_0 = 5\,$MPa, has been assumed. Next, parameters $\tau_{\max} = \theta_0 = 240\,$MPa have been found such that the predicted P–h curve fits the experimental one, and a very good agreement has been achieved (note, however, that the hardening parameters cannot be determined uniquely using the P–h curve alone). The comparison in Fig. 9b made later for the gradient-enhanced model has shown that the agreement for $R = 190\,\mu$m is still very good. Anisotropic hardening parameters have been adopted as $q_{\alpha\beta} = 1$ for coplanar systems and $q_{\alpha\beta} = q = 1.4$ for non-coplanar systems, which are typical values used for fcc metals. Parameter m in the regularized yield function (3.4) has been set equal to $m = 20$.

Parameters a, μ and b in the Taylor formula (2.9), which appear in the gradient-related part of the present model, constitute the last group of material parameters. From the materials science literature, the strengthening coefficient a for fcc crystals in monotonic deformation can be estimated as $a \approx 0.30-0.36$, see SAUZAY and KUBIN [24, page 748], and an intermediate value of $a = 0.33$ has been adopted in this work. Further, following SAUZAY and KUBIN [24, p. 753], the shear modulus μ is assumed as the one for $\langle 110\rangle\{111\}$ slip systems, thus $\mu = (c_{11} - c_{12} + c_{44})/3 = 40.3\,$GPa here. Finally, the Burgers vector modulus in copper is $b = 0.256\,$nm.

It is emphasized that Table 1 provides the complete set of parameters that define a typical model of crystal plasticity *without* any slip-gradient effect. Precisely the same set of parameters defines the gradient-enhanced computational model used here, so that no extra length-scale parameter is introduced. It is recalled that the internal length scale ℓ is fully expressed by standard parameters of the non-gradient hardening law, cf. formula (2.10).

The FE mesh used in the computations is shown in Fig. 6. The size of the FE model is reduced by exploiting the symmetry of the (001)-oriented crystal. In addition to the usual constraints imposed on the displacement components normal to the two symmetry planes, adequate symmetry conditions are enforced on the nonlocal slip increments $\Delta\bar{\gamma}_\alpha$ which constitute global unknowns in the present formulation. Equality of the linked unknowns on the symmetry planes is enforced using the Lagrange multiplier technique. Micro-free boundary conditions $(3.2)_2$ are prescribed on the free surface, including beneath the indenter. The numerical parameter l_h in the PDE governing the non-local slip rates, cf. Eq. (3.1), is set equal to the local element size h, thus $l_h = h$, as motivated by the results shown in Figs. 2, 3 and 5a.

The computational domain is a cube of the edge size of $18a_{\max}$, where $a_{\max}$ is the nominal contact radius corresponding to the maximum penetration depth $h_{\max}$, $a_{\max} = \sqrt{h_{\max}(2R - h_{\max})}$, which is proportional to R for a fixed ratio of $h_{\max}/R$. The mesh is refined towards the indentation zone, and the finest mesh occupies a cube of the edge size of $1.5a_{\max}$, see Fig. 6. Hexahedral eight-node F-bar elements are used [25], and a trilinear interpolation of nonlocal slip increments $\Delta\bar{\gamma}_\alpha$ is employed. At each node there are thus 15 unknowns (3 displacements and 12 nonlocal slip increments). Accordingly, even though the mesh is relatively coarse, the total number of unknowns exceeds 270,000, and the problem is computationally demanding. The direct linear solver (Intel MKL PARDISO) uses over 20 GB of RAM, and one Newton iteration takes about 140 seconds on a 24-core workstation. Further mesh refinement is thus not feasible within our present computational environment. Therefore, we are unable at present to verify convergence of the results with mesh refinement and to estimate the accuracy of the quantitative predictions given below.

The indenter is modelled as a rigid sphere, and frictionless contact is assumed between the indenter and the crystal surface. The impenetrability condition is enforced using the augmented Lagrangian technique [26, 27].

Figure 6 shows the deformed mesh in the vicinity of the indenter. The color map indicates the accumulated slip γ for two selected indenter radii of $2\,\mu$m and $200\,\mu$m. It follows that the distribution of γ is in general only slightly influenced by the variation of R by two orders of magnitude. However, the flow pattern is size dependent which can be seen in Fig. 7 that shows the topography of the residual imprints corresponding to $R = 2$ and $200\,\mu$m. Surface topography is anisotropic with a characteristic pattern of pile-up and sink-in regions, showing less piling-up and more sinking-in with decreasing indenter radius.

The values of the norm $\|\mathbf{G}\|$ of the dislocation density tensor $\mathbf{G}$ are, of course, strongly size-dependent, see Fig. 8. The values are approximately inversely proportional to the indenter radius R. For instance, the maximum values are of the order of 0.008, 0.08 and $0.8\,\mu\text{m}^{-1}$ for the radius R equal to 200, 20 and $2\,\mu$m, respectively (results for the intermediate radius of $20\,\mu$m are not included in Fig. 8). However, there is also a qualitative difference in the pattern of the distribution of $\|\mathbf{G}\|$, which is clearly visible in Fig. 8.

The dependence of hardness on the maximum penetration depth $h_{\max}$ is strongly size dependent, as shown in Fig. 9a. The upper curve in Fig. 9a corresponds to the actual hardness $H = P_{\max}/A$ determined as the ratio of the maximum load $P_{\max}$ to the corresponding (projected) contact area A. The lower curve corresponds to the nominal hardness $H_{\text{nom}} = P_{\max}/A_{\text{nom}}$ in which the load is related to the nominal area $A_{\text{nom}} = \pi a_{\text{nom}}^2$, where $a_{\text{nom}} = \sqrt{h_{\text{res}}(2R - h_{\text{res}})}$ is the nominal contact radius determined in terms of the residual indentation depth h_{res}.

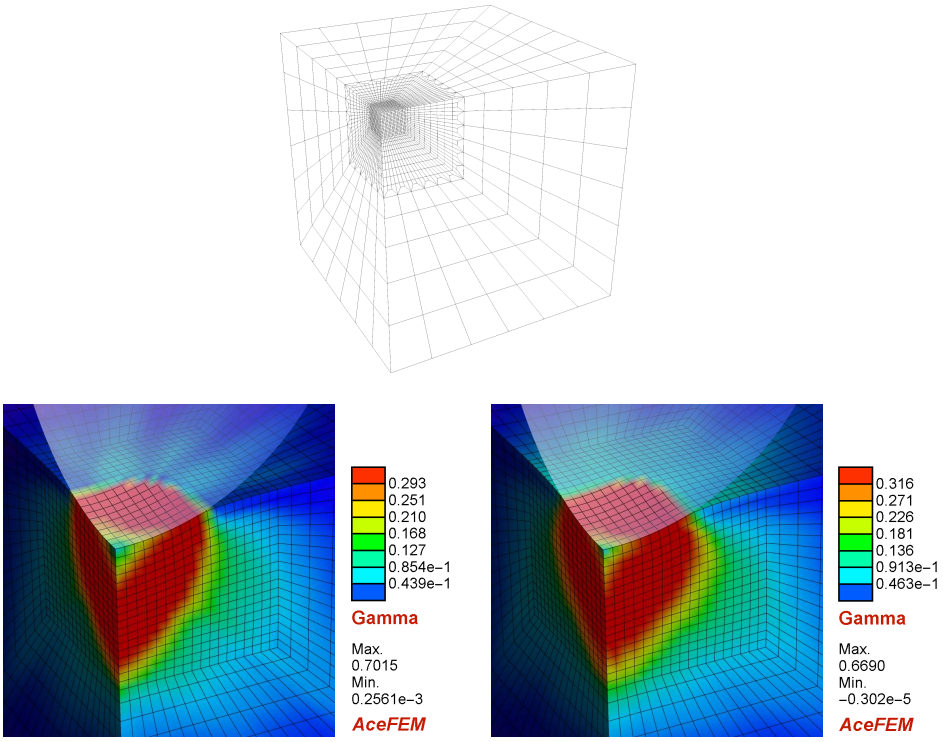

$R = 2\,\mu\text{m}$ $R = 200\,\mu\text{m}$

FIG. 6. Spherical indentation of (001)-oriented Cu single crystal: finite element mesh (top); distribution of accumulated slip γ shown in the deformed configuration in the vicinity of the imprint for $R = 2\,\mu\text{m}$ (bottom-left) and $R = 200\,\mu\text{m}$ (bottom-right). Spherical indenter is indicated by a semi-transparent surface.

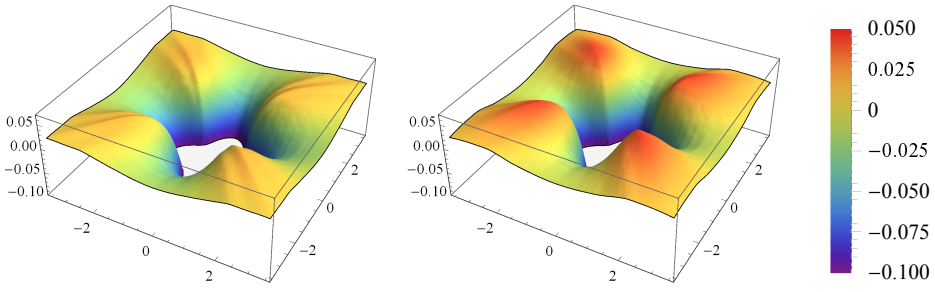

$R = 2\,\mu\text{m}$ $R = 200\,\mu\text{m}$

FIG. 7. Spherical indentation of (001)-oriented Cu single crystal: size-dependent normalized residual impressions. Height is normalized by the residual depth h_{res}, in-plane position is normalized by the nominal residual radius $a_{\text{nom}} = \sqrt{h_{\text{res}}(2R - h_{\text{res}})}$.

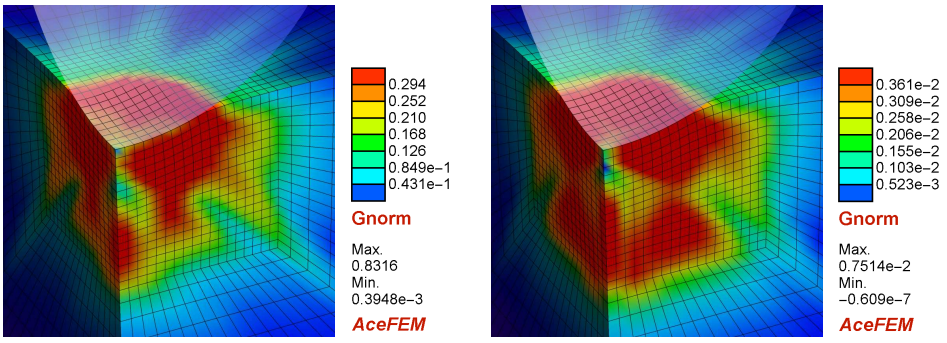

$R = 2\,\mu$m $R = 200\,\mu$m

FIG. 8. Spherical indentation of (001)-oriented Cu single crystal: distribution of the norm $\|\mathbf{G}\|$ of the dislocation density tensor $\mathbf{G}$ shown in the deformed configuration. Spherical indenter is indicated by a semi-transparent surface.

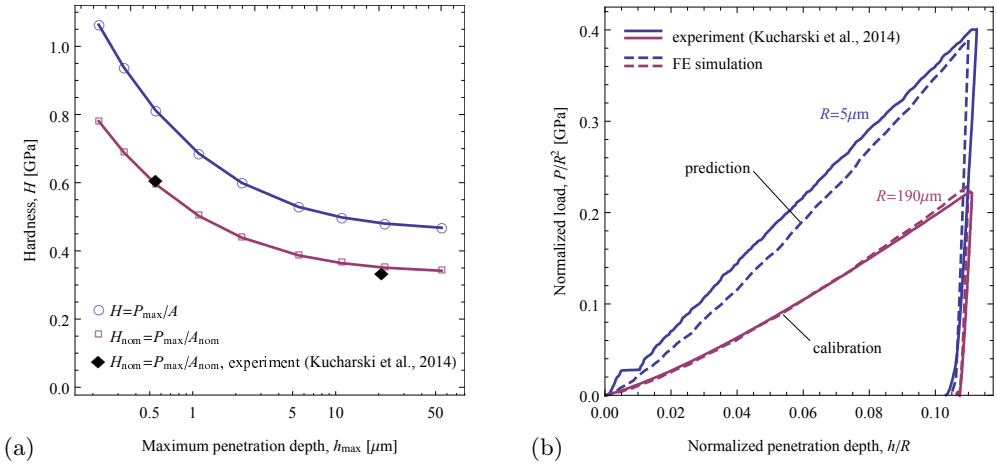

FIG. 9. Spherical indentation of (001)-oriented Cu single crystal: (a) dependence of hardness on the maximum penetration depth at fixed ratio $h_{\max}/R = 0.11$; (b) normalized size-dependent load–penetration curves. Experimental results taken from KUCHARSKI *et al.* [23].

Two experimental points [23] corresponding to $R = 5$ and $190\,\mu$m are also included in Fig. 9a. The contact area was not measured in the experiment, hence the nominal hardness H_{nom} is only reported. Figure 9b shows the comparison of the respective normalized P–h curves. It is recalled that the experimental P–h curve for $R = 190\,\mu$m has been used to calibrate the hardening parameters in the crystal plasticity model (although *without* gradient enhancement). At the same time, the P–h curve for $R = 5\,\mu$m and the corresponding hardness are *predicted*

using the same set of material parameters. The agreement with experiment can be regarded as surprisingly good in view of no freedom to adjust the size effect in the present model.

It is stressed here that the results of spherical indentation reported by KUCHARSKI *et al.* [23] are characterized by high repeatability both for $R = 5\,\mu$m and for $R = 190\,\mu$m, and also for different maximum indentation depths, see Figs. 2 and 3 in [23]. Accordingly, the two experimental P–h curves used in the present work are representative of the indentation behaviour of the high-purity copper crystal tested by KUCHARSKI *et al.* [23].

It is worth noting that, in the experimental P–h curves measured for $R = 5\,\mu$m, the well-known pop-in effect has been observed at the low load of 1–2 mN [23]. This effect is also visible in the experimental curve included in Fig. 9b. It is related to discrete events accompanying the plastic flow at low scales, and is not described by the present continuum model.

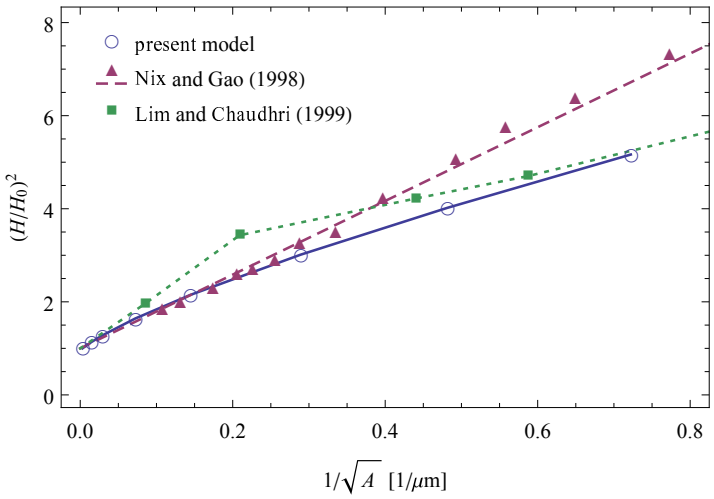

FIG. 10. $(H/H_0)^2$ versus $1/\sqrt{A}$: FE results for spherical indentation of (001)-oriented single crystal copper are compared to experimental results of Berkovich-tip indentation of (111)-oriented single crystal copper (after NIX and GAO [2]) and of polycrystalline OFC copper (after LIM and CHAUDHRI [29]).

Two experimental points as in Fig. 9a (one of them used for calibrating the model) might be treated as insufficient for a convincing verification of the predicted size effect. Therefore, an independent comparison with other experimental indentation data for copper is also provided. Figure 10 shows a comparison to the experimental results reported by NIX and GAO [2], see also MCELHANEY *et al.* [28], for Berkovich-tip nano-indentation of a (111)-oriented single crystal

of annealed copper. NIX and GAO [2] have developed a model which predicts that the squared hardness is a linear function of the inverse of indentation depth and showed that experimental points indeed follow this trend. In order to enable comparison of the results corresponding to different tip geometries, the square root of the contact area is used here as a parameter characterizing the pertinent length scale. In case of a perfect Berkovich indenter, the nominal contact area A is related to the contact depth h by $A = 24.5h^2$, and this formula has been applied to transform the experimental results reported in [2]. The dashed line in Fig. 10 indicates the linear fit of those results, as also reported by NIX and GAO [2], with the hardness H normalized by H_0, the hardness in the size-independent limit of large indentation depths. Additionally, experimental results of LIM and CHAUDHRI [29] obtained for annealed polycrystalline oxygen-free copper (OFC) using Berkovich-tip nano-indentation are also included in Fig. 10.

In the case of the present results, the contact area A is taken directly from the FE simulations, and the hardness corresponding to $R = 500\,\mu$m is adopted as the reference hardness H_0. It can be seen in Fig. 10 that the dependence of $(H/H_0)^2$ on $1/\sqrt{A}$ predicted by the present model is not exactly linear, which is, however, in qualitative accord with some other experimental data, cf. LIM and CHAUDHRI [29], PHARR *et al.* [30]. At the same time, in quantitative terms, the agreement visible in Fig. 10 is quite satisfactory in view of the essential differences between the Berkovich-tip and spherical indentation processes. The main conclusion drawn from the above comparison is that the present computational model formulated in the minimal gradient-enhanced framework of crystal plasticity correctly captures the observed size effect in indentation of Cu single crystals, is spite of the absence of any adjustable length-scale parameter.

5. Conclusion

The model of gradient-enhanced crystal plasticity proposed in Part I [1] has been implemented in a finite element code and applied to three-dimensional simulations of fcc single crystals. The major aim of the simulations has been to verify whether the model correctly captures the experimentally observed indentation size effect. The comparison has been performed for a Cu single crystal, and the agreement has been found satisfactory. This can be interpreted as a verification that the internal length scale (2.10) in combination with the effective slip-rate gradient (2.12) in the incremental hardening law (2.6) lead to predictions of size effects that are in accord with experiment. Of course, further work is needed to confirm validity of that conclusion by other examples.

The model has been incorporated into the framework of classical continua, and the gradients of slip rates enter the formulation only through the enhanced hardening law. It was thus not immediate how to compute, in the finite-element

framework, the slip-rate gradients and also how to impose the boundary constraints on slip-rates. To address these issues, a finite-element treatment has been developed in which non-local slip-rates are introduced that provide a global continuous approximation of the respective local Gauss-point quantities. The gradients of those non-local slip-rates are then used in the enhanced hardening law.

As another verification of the proposed approach, a one-dimensional problem of shearing of a constrained half-space has been studied. It has been shown that the finite-element solution converges to the analytical one as the mesh size decreases. The regularizing effect achieved by introducing the non-local slip-rates has also been demonstrated in the case of shearing of a constrained strip. The corresponding non-regularized analytic solution exhibits a kink in the profile of the accumulated slip. It has been shown that, in the finite-element solution, the profile of the accumulated non-local slip is smooth, but, at the same time, it provides a consistent approximation of the non-smooth analytic solution.

Acknowledgement

This work has been supported by the National Science Center (NCN) in Poland through Grant No. 2014/13/B/ST8/04286.

References

1. H. PETRYK, S. STUPKIEWICZ, *A minimal gradient-enhancement of the classical continuum theory of crystal plasticity. Part I: The hardening law*, Arch. Mech. **68** (2016), 459–485.
2. W.D. NIX, H. GAO, *Indentation size effects in crystalline materials: a law for strain gradient plasticity*, J. Mech. Phys. Solids **46** (1998), 411–425.
3. P. CERMELLI, M.E. GURTIN, *On the characterization of geometrically necessary dislocations in finite plasticity*, J. Mech. Phys. Solids **49** (2001), 1539–1568.
4. J.F. NYE, *Some geometrical relations in dislocated crystals*, Acta Metall. **1** (1953), 153–162.
5. E.P. BUSSO, F.T. MEISSONNIER, N.P. O'DOWD, *Gradient-dependent deformation of two-phase single crystals*, J. Mech. Phys. Solids **48** (2000), 2333–2361.
6. L.P. EVERS, W.A.M. BREKELMANS, M.G.D. GEERS, *Non-local crystal plasticity model with intrinsic SSD and GND effects*, J. Mech. Phys. Solids **52** (2004), 2379–2401.
7. M. EKH, M. GRYMER, K. RUNESSON, T. SVEDBERG, *Gradient crystal plasticity as part of the computational modelling of polycrystals*, Int. J. Num. Meth. Engng. **72** (2007), 197–220.
8. S. BARGMANN, B.D. REDDY, B. KLUSEMANN, *A computational study of a model of single-crystal strain-gradient viscoplasticity with an interactive hardening relation*, Int. J. Sol. Struct. **51** (2014), 2754–2764.

9. S. WULFINGHOFF, T. BOEHLKE, *Equivalent plastic strain gradient enhancement of single crystal plasticity: theory and numerics*, Proc. R. Soc. A **468** (2012), 2682–2703.

10. R.H.J. PEERLINGS, R. DE BORST, W.A.M. BREKELMANS, J.H.P. DE VREE, *Gradient enhanced damage for quasi-brittle materials*, Int. J. Num. Meth. Engng. **39** (1996), 3391–3403.

11. M.G.D. GEERS, *Finite strain logarithmic hyperelasto-plasticity with softening: a strongly non-local implicit gradient framework*, Comp. Meth. Appl. Mech. Engng. **193** (2004), 3377–3401.

12. M. ARMINJON, *A regular form of the Schmid law. Application to the ambiguity problem*, Textures and Microstructures **14–18** (1991), 1121–1128.

13. W. GAMBIN, *Refined analysis of elastic-plastic crystals*, Int. J. Sol. Struct. **29** (1992), 2013–2021.

14. J. MANDEL, *Plasticité classique et viscoplasticité*, CISM course No. **97**, Springer, Wien, 1971.

15. J.W. HUTCHINSON, *Bounds and self-consistent estimates for creep of polycrystalline materials*, Proc. R. Soc. Lond. A **348** (1976), 101–127.

16. D. PEIRCE, R.J. ASARO, A. NEEDLEMAN, *Material rate dependence and localized deformation in crystalline solids*, Acta Metall. **31** (1983), 1951–1976.

17. C. MIEHE, *Exponential map algorithm for stress updates in anisotropic multiplicative elastoplasticity for single crystals*, Int. J. Num. Meth. Engng. **39** (1996), 3367–3390.

18. P. STEINMANN, E. STEIN, *On the numerical treatment and analysis of finite deformation ductile single crystal plasticity*, Comp. Meth. Appl. Mech. Engng. **129** (1996), 235–254.

19. J. KORELC, *Multi-language and multi-environment generation of nonlinear finite element codes*, Engineering with Computers **18** (2002), 312–327.

20. C.S. HAN, H. GAO, Y. HUANG, W.D. NIX, *Mechanism-based strain gradient crystal plasticity—II. Analysis*, J. Mech. Phys. Solids **53** (2005), 1204–1222.

21. J.Y. SHU, N.A. FLECK, E. VAN DER GIESSEN, A. NEEDLEMAN, *Boundary layers in constrained plastic flow: comparison of nonlocal and discrete dislocation plasticity*, J. Mech. Phys. Solids **49** (2001), 1361–1395.

22. E. BITTENCOURT, A. NEEDLEMAN, M.E. GURTIN, E. VAN DER GIESSEN, *A comparison of nonlocal continuum and discrete dislocation plasticity predictions*, J. Mech. Phys. Solids **51** (2003), 281–310.

23. S. KUCHARSKI, S. STUPKIEWICZ, H. PETRYK, *Surface pile-up patterns in indentation testing of Cu single crystals*, Exp. Mech. **54** (2014), 957–969.

24. M. SAUZAY, L.P. KUBIN, *Scaling laws for dislocation microstructures in monotonic and cyclic deformation of fcc metals*, Progress Mater. Sci. **56** (2011), 725–784.

25. E.A. DE SOUZA NETO, D. PERIĆ, M. DUTKO, D.R.J. OWEN, *Design of simple low order finite elements for large strain analysis of nearly incompressible solids*, Int. J. Sol. Struct. **33** (1996), 3277–3296.

26. P. ALART, A. CURNIER, *A mixed formulation for frictional contact problems prone to Newton like solution methods*, Comp. Meth. Appl. Mech. Engng. **92** (1991), 353–375.

27. J. LENGIEWICZ, J. KORELC, S. STUPKIEWICZ, *Automation of finite element formulations for large deformation contact problems*, Int. J. Num. Meth. Engng. **85** (2011), 1252–1279.

28. K.W. MCELHANEY, J.J. VLASSAK, W.D. NIX, *Determination of indenter tip geometry and indentation contact area for depth-sensing indentation experiments*, J. Mater. Res. **13** (1998), 1300–1306.

29. Y.Y. LIM, M.M. CHAUDHRI, *The effect of the indenter load on the nanohardness of ductile metals: an experimental study on polycrystalline work-hardeded and annealed oxygen-free copper*, Phil. Mag. A **79** (1999), 2979–3000.

30. G.M. PHARR, E.G. HERBERT, Y. GAO, *The indentation size effect: A critical examination of experimental observations and mechanistic interpretations*, Annu. Rev. Mater. Res. **40** (2010), 271–292.

Received November 28, 2016.